# Structural analysis of magnetic nanocomposites based on chitosan

Gianina A. Kloster[a], Diego Muraca[b], Oscar Moscoso Londoño[b,c], Marcelo Knobel[b], Norma E. Marcovich[a], Mirna A. Mosiewicki[a,*]

[a] *Instituto de Investigaciones en Ciencia y Tecnología de Materiales (INTEMA), Facultad de Ingeniería, Universidad Nacional de Mar del Plata, CONICET, Mar del Plata, Argentina*
[b] *Instituto de Física Gleb Wataghin (IFGW), Universidade Estadual de Campinas, UNICAMP, Campinas, São Paulo, Brazil*
[c] *Universidad Autónoma de Manizales, Facultad de Ingeniería, Antigua Estación del Ferrocarril, Manizales, Colombia*

ABSTRACT

This work investigates the structure and magnetic properties of chitosan based films with different contents of magnetic nanoparticles (MNPs) of around 10 nm as well as the effects of the addition of glycerol as plasticizer. Synthesized MNPs were dispersed in the chitosan film forming solution by ultrasonication and then composite films were obtained by casting. From the morphological analysis, a bimodal distribution of clusters was detected; the larger ones seem to be present mostly in the plasticized samples. Regarding the mechanical behavior of the samples, for the non-plasticized samples the outstanding increase in modulus and strength with the increasing content of MNP was explained by a strong interfacial adhesion and very good particles dispersion into the chitosan matrix. This fact was also supported by the model applyed to the strength as a function of the volume fraction of MNP.

Regarding magnetic properties, all nanocomposite films evidenced systems with particles of strong dipolar interactions that lead to blocking and irreversibility temperatures close to room temperature (RT). Even though the isothermal magnetization results showed that the particles in the nanocomposite films behave as superparamagnetic at the highest analyzed temperature (RT). Langevin model as well as FESEM and SAXS analysis supported the hypothesis that the formation of aggregates with different features dominates the magnetic response through collective behavior, mainly in the plasticized films.

## 1. Introduction

The study and use of nanocomposites based on biopolymers with a magnetic disperse phase is an important area of research in constant growth due to potential applications, including uses in biomedicine, biotechnology and wastewater treatment [1,2], for example. The choice of a polymer with chelating properties such as chitosan has shown very promising results in the treatment of contaminated water with heavy metal ions, herbicides and dyes [3–5]. Chitosan is a biodegradable polymer extracted from the deacetylation of the chitin, major component of crustacean's shells and fungal biomass. This cationic polysaccharide, composed by β-(1,4)-2-amino-2-deoxy-D-glucopyranose units and small quantity of N-acetyl-D-glucosamine residues [6,7], displays interesting properties including biocompatibility, non-toxicity, good film forming ability, antibacterial and antifungal activity [8]. It contains several reactive groups that interact with metal ions through various mechanisms depending on the involved ion, the pH, and solution composition [9], acting as an excellent adsorbent agent.

The incorporation of iron oxide nanoparticles (NPs) as a disperse phase allows obtaining a nanocomposite that could provide interesting properties. For example, these nanocomposites could be easily removed from water with the help of an external magnet [10], while remaining environmental friendly due to the low toxicity and biocompatible characteristics of the iron oxides [11]. The magnetic properties of the composites will be determined principally by the nanoparticle magnetic properties and their interactions. When the size of the iron oxide NPs is below a critical size ($< 15$ nm [12]), they could exhibit superparamagnetic behavior and thus, even embedded in a polymeric matrix, the magnetic moment of each NP will follow the direction of the applied magnetic field allowing to move or attract the nanocomposite with an external magnetic field. In this line, Zhuang et al. [13] have synthesized $Fe_3O_4-SiO_2-SrHAp$ microspheres for the immobilization of Pb (II), which were simply collected from water by magnetic separation.

The interaction between chitosan and iron oxides NPs is explained through complex mechanisms of electrostatic forces and interactions

occurring between polar groups [14–18]. Different methods of synthesis have been applied to obtain chitosan/iron oxide nanocomposites. For instance, Bezdorozhev et al. [19] have reported the synthesis of magnetite-chitosan nanostructures by the chemical precipitation of magnetite NPs in the presence of chitosan. In that work, the authors vary some synthesis parameters to study their influence on the nanoparticle morphology. Singh and co-workers [20] fabricated nanocomposite films based on hydrothermally prepared hematite ($\alpha$-$Fe_2O_3$) NPs and chitosan using glycolic acid as organic surfactant. According to the authors, the obtained NPs had an irregular spheroidal shape with a mean diameter of 110 nm. The coating of magnetic particles has been extensively used to control or tune their agglomeration and to assist the size control of particles due to cross-linking among NPs with chitosan, fact extremely important in order to achieve the desired physical or chemical behavior. A good example of this is the work published by Bhatt et al. [21], where iron oxide NPs were synthesized separately (via the hydrothermal process) and then dispersed into the chitosan solution by ultrasonication, resulting in materials with new electrical and magnetic properties.

However, and depending on the application envisaged for the magnetic nanocomposite, the formation of clusters from individual nanoparticles could present some advantages in comparison with systems containing more homogeneously dispersed magnetic nanoparticles. The magnetic response of the clusters is different than that of the individual particles. When the particles are close enough, the magnetic moment of each particle will be affected by those of the neighbor ones due to magnetic dipolar interactions. Thus, the magnetic moment of an agglomerate of magnetic nanoparticles will be different from the individual magnetic moment of each nanoparticle [22]. However, results regarding the most efficient nanoparticles configuration (agglomerated or totally dispersed) are still controversial. While it is expected that fully dispersed nanoparticles should be the best nanoparticle configuration, several reports show that inter-particle dipole interactions in clusters can contribute positively to magnetic hyperthermia or magnetic heating properties [23].

On the other hand, the method of preparation not only changes the dispersion and size of the particles and/or clusters into the matrix. Different methods of synthesis lead to different degrees of interaction of the particles with the matrix and the amount of plasticizer that can be retained into the film. The synthesis of magnetic particles and posterior incorporation into the chitosan solution could lead to a weaker interaction between matrix and particles/clusters than the "in situ" synthesis [24] and in this way, the magnetic entities would be freer to react in the presence of an external magnetic field. In addition, this last method allows a better control of the amount of plasticizer required in the films that can significantly affect some specific properties (for example, mechanical properties) in comparison with that of the nanocomposite films prepared by the "in situ" method.

In a previous work, we reported the obtaining of chitosan/MNP nanocomposite films via "in situ" synthesis of magnetite [25]; both mechanical and magnetic properties were discussed and explained in terms of the matrix composition and nanoparticle concentration. In this work, magnetic iron oxides NPs were incorporated to a chitosan solution and dispersed by ultrasonication to obtain magnetic nanocomposite films. NPs were obtained by a simple iron oxide alkaline precipitation method, followed by washings and solvent elimination via lyophilization. The effects of the glycerol (plasticizer) and magnetic nanoparticles concentration on the physical, morphological, mechanical and magnetic properties of the films are presented and discussed. Besides, the information about these nanostructured materials was complemented by SAXS analysis by means of fitting experimental results with appropriate models.

## 2. Experimental procedures

### 2.1. Materials

Chitosan in powder form (degree of deacetylation 98%, Mv = $1.61 \times 10^5$ g/mol) was supplied by Parafarm. Glycerol (G), purchased from DEM Mar del Plata, was used as plasticizer. Ferric chloride hexahydrate ($FeCl_3.6H_2O$), ferrous sulphate heptahydrate ($FeSO_4.7H_2O$) and ammonium hydroxide (25% $NH_3$) were obtained from Aldrich. All the samples were prepared using commercially available reagents.

### 2.2. Methods

#### 2.2.1. Synthesis of magnetic iron oxides nanoparticles

The iron oxide NPs were obtained by an alkaline co-precipitation method adapted from that developed by Massart and Cabuil [26]. In brief, 4.8 g of $FeSO_4.7H_2O$ and 9.32 g of $FeCl_3.6H_2O$ (molar ratio $Fe^{+2}$:$Fe^{+3}$ = 1:2) were dissolved in approximately 40 mL of distilled water. Once the solution was perfectly homogenized, 15 mL of $NH_4OH$ was added drop by drop in order to avoid or minimize the MNPs aggregation. The suspension was stirred for 15 min, allowing the complete precipitation of MNPs. After this time and with the help of a magnet placed out of the flask, several washes with distilled water were made until neutral pH. Then, the wet particles were placed into a Petri plate and lyophilized to eliminate the water. Finally, the obtained powder was kept into a dark colored glass container.

#### 2.2.2. Preparation of composite films

Chitosan solution (2% w/v) was prepared by dissolving chitosan powder in aqueous acetic acid solution (1% v/v) by magnetic stirring at room temperature. Glycerol, in a weight ratio glycerol/chitosan equal 0.3, was also added to the solution when applicable. Selected amounts of MNPs were incorporated to the polymer solution to prepare nanocomposite films. Film forming suspensions were obtained by manually mixing MNPs with chitosan (or chitosan/glycerol) solution, followed by ultrasonication for 2 h (Elmasonic P60H sonicator with a frecuency of 37 kHz and a power of 150 W). As it is know that ultrasonication can cause some degradation of the bio polymer, neat chitosan and chitosan/glycerol solutions, used to prepare control films (0% MNPs), were also sonicated. Then, the suspensions were poured into Petri dishes (diameter = 14 cm) and dried in a convective oven at 35 °C for 24 h (solvent casting). The actual MNP content of the films was determined by thermogravimetric analysis, as indicated in the following sections.

The obtained films, with thickness in the range of 200–300 μm, were kept in a closed container containing dried silica gel at room temperature (23 ± 2 °C) until testing. Non-plasticized film samples were labeled as S0, S1, S2, S3, S4, S5, while a "G" was added at the end of the acronym for plasticized samples (i.e. S0G, S1G, S2G, S3G, S4G and S5G).

#### 2.2.3. Characterization of MNPs and composite films
##### 2.2.3.1. Film thickness.
The thickness of the films was measured with a 0–25 mm manual micrometer with an accuracy of ± 0.01 mm at least at five random locations for each film. The reported values are the average of those individual measurements.

##### 2.2.3.2. X-ray diffraction (XRD).
The crystal structure of the MNPs was investigated using CuK$\alpha$ radiation ($\lambda$ = 1.5418 A) in a PANalytical X'Pert Pro diffractometer operated at 40 kV, 300 mA and 0.6 °C/min.

##### 2.2.3.3. Transmission electron microscopy (TEM).
TEM analysis of the MNPs was performed on a TEM-FEG (JEM 2100F) field-emission gun transmission electron microscope (voltage: 200 kV). The images were acquired using a Gatan, Orius SC600/831 camera at different resolutions. The particles were dispersed in Milli-Q water and

sonicated during 15 min. The samples for microscopy observation were prepared by drying a drop of this suspension during 24 h at room temperature on a Ted Pella ultrathin cooper film on a holey carbon. The obtained images were analyzed using ImageJ free software.

*2.2.3.4. Small-angle X-ray scattering (SAXS).* SAXS experiments were performed on SAXS1 beamline at the Brazilian Synchrotron Light Laboratory (LNLS), Centro Nacional de Pesquisa em Energia e Materials (CNPEM), Campinas, Brazil. The measurements were carried out at room temperature. The scattering intensity was recorded as function of momentum transfer vector $q$ ($q = 4\pi \sin\theta/\lambda$), in a range from 0.1 to 5.0 nm$^{-1}$, being $\theta$ the scattering angle and $\lambda$ the wavelength = 1.822 Å.

*2.2.3.5. Thermogravimetric analysis (TGA).* Thermogravimetric tests of the films were performed in a TGA-40 Shimadzu Thermogravimetric Analyzer at a heating rate of 10 °C/min under air atmosphere (35 mL/min) from room temperature to 900 °C. Samples tested were previously dried in a vacuum oven during 2 h at 60 °C followed by 22 h at 40 °C, to remove traces of water absorbed during storage.

*2.2.3.6. Field emission scanning electron microscopy (FESEM).* The cryofractured surface (thickness) of the films were analyzed with a Carl Zeiss Supra 40 Gemini, Field Emission Scanning Electron Microscope (FESEM) equipped with an energy dispersive X-ray spectroscopy (EDS) attachment for elemental analysis.

*2.2.3.7. Tensile properties.* Tensile tests were performed at room temperature (23 ± 2 °C) using an Instron Universal Testing Machine model 8501. The specimens were cut into strips of 5 × 25 mm. Five specimens from each film were tested from a minimum of three films per sample. Crosshead speed was set at 10 mm/min. The ultimate strength ($\sigma_u$), elongation at break ($\varepsilon_b$) and elastic modulus ($E$) were calculated as described in ASTM D638-94b (ASTM, 1994). Prior to running mechanical tests, films were conditioned for 72 h at 65 ± 5% relative humidity at room temperature.

*2.2.3.8. Magnetic characterization.* The magnetic properties of the composite film were obtained using a commercial SQUID magnetometer (Quantum Design, MPMS XL). Both isothermal magnetization curves ($M$ *vs.* $H$) as well as the temperature dependence of magnetization ($M$ *vs.* $T$) were obtained. The $M$ *vs.* $H$ curves were recorded at 2 and 300 K in a magnetic field range of ± 1T. The M vs. T curves were recorded under the zero-field-cooling and field-cooling (ZFC/FC) protocols with a static magnetic field of 50 Oe. Samples used for these tests were previously conditioned in a closed container with silica gel until they reached their equilibrium moisture content (about 5–7 wt.%).

## 3. Results and discussion

### 3.1. Structural studies of the magnetic particles

Fig. 1 shows representative transmission electron micrographs of the synthesized iron oxide NPs; the inset of Fig. 1(a) shows the size distribution obtained by counting more than one hundred particles. From the analysis of the histogram, an average particle diameter of 9.5 ± 2 nm with a narrow size distribution was calculated (full line represents the best fit according to a lognormal size distribution).

Fig. 1(a and b) reveals a moderate agglomeration of the particles, as can be expected for a set of magnetic NPs without surface treatments/surfactant [27]. It is also noticed that not all the particles have a spherical shape, some of them presenting shape irregularities. Fig. 1(c) shows a HR-TEM image of a selected nanoparticle. Fast Fourier Transform (FFT) was used to estimate the Bragg plane distances on the HR-TEM image allowing to identify the (113) and (044)

crystallographic planes corresponding to the magnetite ($Fe_3O_4$) and/or maghemite ($Fe_2O_3$) spinel-inverse [28].

X-ray diffraction pattern of the synthesized particles was also analyzed (Figure S1, supplementary information). The positions and relative intensities of the diffraction peaks agree with those of a pure face-centered cubic (fcc) spinel-inverse iron oxide phase corresponding to the standard crystal of magnetite and/or maghemite [29–31]. The crystal size (D) was determined using Scherrer's equation [32–34], from which a value of D = 9.5 nm was obtained.

Despite that "crystallite size" is not necessarily synonymous of "particle size", this method gives an estimation of the diameter of the magnetic particles [27]. Notice that the obtained value is close to those determined from TEM images.

Small-angle X-ray scattering (SAXS) technique was used to analyze the morphological features of magnetic NPs before they are loaded into the chitosan matrices. Figure S2a in supplementary information presents the SAXS scattering patterns obtained from the synthesized NPs. According to the range of $q$ parameter selected for the measurement, the NPs that could be characterized have sizes ranging between $\pi/q_{max}$ = 1 nm to $\pi/q_{min}$ = 30 nm. From linear Guinier law at low $q$ region (Figure S2b, supplementary information) the radius of gyration, $Rg$, was calculated as 6 nm [35,36].

Then, if the NPs are mostly spherical, an average diameter, $Dg$, of 15.4 nm was estimated indicating that possibly small aggregation of primary particles occurs when they are in a colloidal suspension. The scattering intensity in the Porod region presents a slope close to −4, which corresponds to individual particles with smooth surfaces [36,37].

### 3.2. Characterization of the nanocomposites films

Thermogravimetric measurements were carried out in air atmosphere in order to determine the content of MNPs effectively incorporated into the films and to study the thermal degradation of the nanocomposites. From the residual mass left at 800 °C, the iron oxide content was obtained considering that the residual char corresponds to chitosan (or chitosan + glycerol) and ferric oxide, since oxidation process of magnetite into ferric oxide due to heating occurs in the range of 130–330 °C, as was reported elsewhere [38,39]. The residual mass, corresponding to the matrix, was subtracted proportionally from the residual char of the composite samples and the difference was converted to magnetite mass. These calculations are listed in Table 1, as actual magnetite content. It should be mentioned that during the preparation process not all the MNP could be successfully loaded in the film forming solutions (i.e. forming a stable colloidal suspension), thus part of the magnetic solute remained at the bottom of the flask where the suspension was prepared, not being transferred to the Petri dish (mold).

Fig. 2 presents the TGA curves for selected composite films prepared from neat and plasticized chitosan (S0, S3, S5, S0G, S3G, S5G). Both matrices (films without MNP) exhibit three main stages of weight loss. The first one is attributed to loss of absorbed water due to the hydrophilic character of the chitosan and, in the case of the plasticized sample, also to the loss of the free glycerol. For this reason, the loss of weight of the plasticized samples at relatively low temperature is larger than the corresponding to neat chitosan films. The second step of weight loss, with maximum degradation rate at around 270 °C corresponds to the chemical degradation and deacetylation of chitosan [40]. The last step observed between ~480 and 630 °C corresponds to the oxidative degradation of the carbonaceous residue, which is formed during the second step [16].

Table 1 presents the temperature at the maximum degradation rate and the initial decomposition temperature of the last degradation step. It is clear that the plasticizer produces a movement of the third step to higher temperatures. Higher thermal stability with the presence of glycerol in films of chitosan was also reported in the works of Debandi and co-workers (2016) [41] and Fundo et al. (2015) [42]. In the last
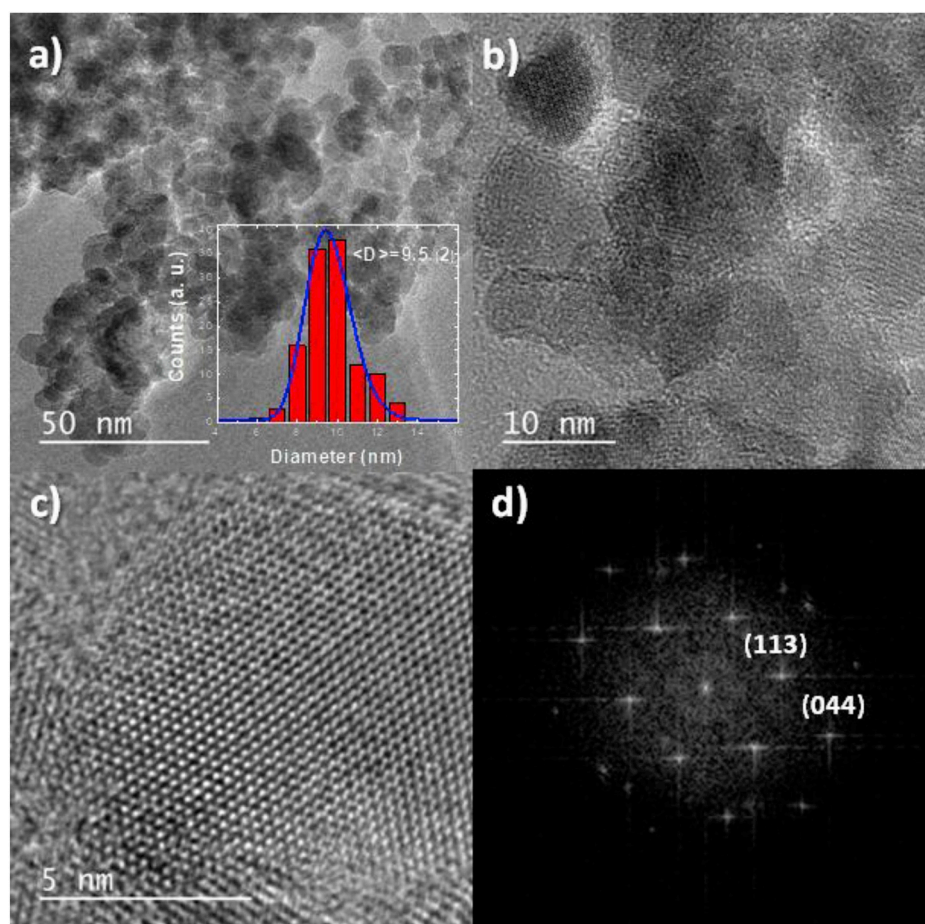
**Fig. 1.** (a)–(b) Transmission electron microscopy at different magnifications (right corner inset of Fig. 1a), size distribution of these MNPs), (c) HR-TEM of selected MNP, (d) FFT of the HR-TEM on figure (c).

**Table 1**

Actual content of MNP of the films, initial temperature (Ti) and temperature at maximum degradation rate (Tm) of the 3rd thermal degradation step. All data were obtained from TGA analysis in air atmosphere.

| Sample | MNPs actual content (wt.%) | Ti (3rd step) (°C) | Tm (3rd step) (°C) |
|--------|----------------------------|--------------------|--------------------|
| S0 | 0.00 | 532.0 ± 16.9 | 574.0 ± 22.6 |
| S1 | 1.2 ± 0.2 | 481.5 ± 17.7 | 510.0 ± 14.1 |
| S2 | 2.2 ± 0.3 | 467.5 ± 2.1 | 489.0 ± 1.4 |
| S3 | 3.0 ± 0.5 | 437.5 ± 2.1 | 459.0 ± 1.4 |
| S4 | 3.7 ± 0.2 | 409.7 ± 8.0 | 436.3 ± 14.6 |
| S5 | 5.8 ± 0.4 | 398.0 ± 7.2 | 416.3 ± 4.0 |
| S0G | 0.00 | 552.0 ± 22.6 | 589.5 ± 19.0 |
| S1G | 1.3 ± 0.0 | 509.0 ± 5.6 | 531.0 ± 2.8 |
| S2G | 1.6 ± 0.3 | 489.0 ± 7.1 | 510.0 ± 18.3 |
| S3G | 3.0 ± 0.4 | 517.5 ± 0.7 | 528.0 ± 8.4 |
| S4G | 3.6 ± 0.4 | 452.5 ± 3.5 | 469.0 ± 11.3 |
| S5G | 4.7 ± 0.3 | 408.0 ± 8.4 | 430.5 ± 0.7 |

case, authors reported that plasticizer addition increased the melting enthalpy, i.e., increases the samples crystallinity, and attributed this effect to glycerol interaction with chitosan chains indicating that the H-bonds stabilize chitosan crystals. They also noticed that the main peak shifted to higher melting temperatures when increasing plasticizer concentration, which correlated well with other published results [43] and may be also related with an increase of the strength of the H-bonds stabilizing chitosan crystals in the presence of plasticizer, as indicated by Okuyama et al. (1997) [44]. Thus, although part of the glycerol is lost in the first stage of degradation, as was mentioned above, a high percentage remain retained in the polymer structure because of these

strong intermolecular interactions developed with chitosan. As a consequence, plasticized samples are not only more crystalline than unplasticized films, but also contain more stable crystals that start to degrade at higher temperature. Moreover, due to the different initial structures of plasticized and non plasticized films, there should be diffusive changes in the volatile products and pyrolysis wastes generated in the second step of degradation that also could affect the degradation pattern of the last step.

Regarding magnetic composite films, it can be observed that the addition of MNP only slightly affects the degradation at the first and second steps. However, the temperatures related with the third step (temperature at the maximum degradation rate and the initial decomposition temperature) decrease significantly as the iron oxide content increases (Table 1). This effect was also noticed in other related works, for example, in our previous work we associated it with the changes in the conformation of the chitosan surrounding the particles in comparison with the chitosan in bulk [25]. Soto et al. (2018) [45] also reported a decreased thermal stability, in comparison with that of the neat polymeric matrix, in their nanocomposite films based on a commercial shape memory polyurethane and different contents of magnetic iron oxides, which was associated to the increase in the thermal conductivity and thermal diffusivity of the material due to the addition of MNP. Additionally, Bertolino et al. (2018) [46] found that their nanocomposites based on chitosan and halloysite nanotubes, also prepared by casting, did not present any thermal stabilization effect due to the presence of particles. They related this fact to the adsorption of positive biopolymer on the halloysite external surface, also with positive charge. In our case it should be noticed that chitosan - MNP suspensions were prepared in acetic acid solutions (i.e. acidic pH) and in this condition
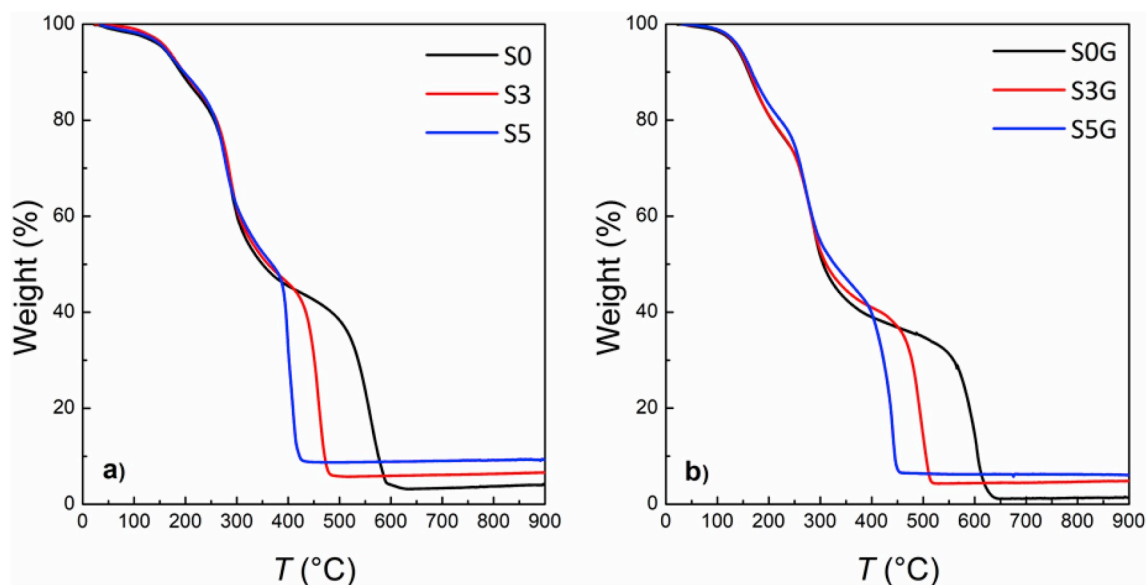
**Fig. 2.** TGA curves of nanocomposite films: (a) non-plasticized; (b) containing 30 wt% glycerol.

both, chitosan and Fe$_3$O$_4$ nanoparticles, are also positively charged (i.e. the isoelectric point of the MNP is around 6.85 as reported in Xu et al. (2006) [47], Regazzoni et al. (1981) [14] and Kloster et al. (2017) [48]). Moreover, Moeini et al. (2018) [49] indicated for chitosan based microbeads cross-linked by using sodium tripolyphosphate (TPP) that some domains in which the electrostatic repulsion prevailed could trigger a less packed structure more prone to the thermal degradation, which match exactly the present case. In this sense, these changes in the macromolecular backbone structure of the polymer would induce the weakening of the attractive intra-inter-molecular hydrogen bonds and thus, chitosan macromolecular chains would result more exposed to the random splitting of the glycosidic bonds that takes place during the thermal degradation process. Additionally, Ziegler-Borowska et al. (2016) [50] indicated that a slight decrease in the initial decomposition temperature of the magnetite-modified chitosan nanocomposite particles, in comparison with the respective chitosan derivatives (including unmodified chitosan), was observed in all cases and attributed to the presence of Fe$_3$O$_4$. They concluded that magnetite exhibited a catalytic action on the thermal degradation of chitosan and its derivatives, but did not outline any explanation for this behavior. Moreover, in a previous publication (Ziegler-Borowska et al., 2015) [51] they emphasized that magnetite NPs enhances thermo-oxidative degradation of polymers. In brief, we believe that the decreased thermal stability of the nanocomposites, in comparison to those of the corresponding neat matrices, is due to several complex and interrelated factors.

The direct observation of the non-plasticized and plasticized films (images not shown) denotes that the samples become darker with the increase of the content of iron oxides, due to the strong coloration of the added magnetic particles. However, inhomogeneous color was detected, indicating the existence of zones with more concentration of magnetic solute. In comparison to other methods, the synthesis protocol used in this work to incorporate MNP into the matrices (synthesis of MNP and posterior dispersion by sonication in the film forming solution), seems to promote the cluster formation, resulting in lesser homogeneous films, when they are compared to those synthesized using "in situ" procedures [25,52].

FESEM analysis was performed to characterize the morphology of the composites. Fig. 3 shows images from the cross section of plasticized and non-plasticized films obtained by fragile fracture under liquid air. Different sizes of structures related to iron oxide particles can be observed, ranging from small agglomerates to relatively large clusters formed by collapsed individual particles. As expected, the images show

a clear increase in density of white particles (associated to dispersed magnetic entities) as the content of particles increases. On the other hand, although the images presented in Fig. 3 seem to denote bigger structures for the plasticized films, the technique did not allow determining an unequivocal trend regarding the size of agglomerates.

Tensile properties of the films are summarized in Table 2. Both, modulus and strength of the non-plasticized films increase with the increment of MNP content. As an example, the addition of MNP into non-plasticized matrix in the sample S5 generates a 52.8% of increase in the modulus and 37% in the ultimate stress respect to the neat matrix. The increase of modulus is related with the high rigidity of the MNP in comparison with that of the polymeric matrix and can be expected if the particles or their clusters are homogeneously distributed and no pores or bubbles are generated during drying of the composite. On the other hand, the increase in ultimate stress of nanocomposites in comparison with that of the neat matrix is expected only when the filler acts as reinforcement, which normally takes place for fillers highly compatible and/or interacting with the polymeric matrix [53,54]. Anyhow, the standard deviation of both measurements is high for some of the samples and thus probably the unique significant difference can be found by comparing S5 composite with the neat matrix.

Pukanszky and co-workers [55] assumed that the yield stress of a filled polymer is determined by the decrease of the effective load bearing cross section of the matrix due to filler and by the polymer-filler interaction. They proposed the following equation to relate the strength of the particulate composite with the volume fraction of filler:

$$\sigma_{film} = \sigma_{matrix}\left(\frac{1 - V_{MNP}}{1 + 2.5 \cdot V_{MNP}}\right) \cdot exp(B \cdot V_{MNP)} \tag{1}$$

where $\sigma_{film}$ and $\sigma_{matrix}$ are the ultimate stresses of the nanocomposite film and the unfilled matrix, respectively, $V_{MNP}$ is the volume fraction of the magnetic solute into the film (MNP in this case) and $B$ is a parameter related with the specific area and density of the filler as well as the thickness and strength of the interface characterizing the interfacial interaction filler-matrix, which serve also as a measurement of the reinforcement efficiency of the filler [40].

If $B = 0$ the filler acts as a void and no adhesion and no stress transfer take place at the filler-matrix interface. For $B > 3$ the filler-matrix interface is good, and an effective reinforcing effect is obtained.

The volume fraction of MNP ($V_{MNP}$) can be calculated, assuming additivity of the volumes ($\nu$) as follow:
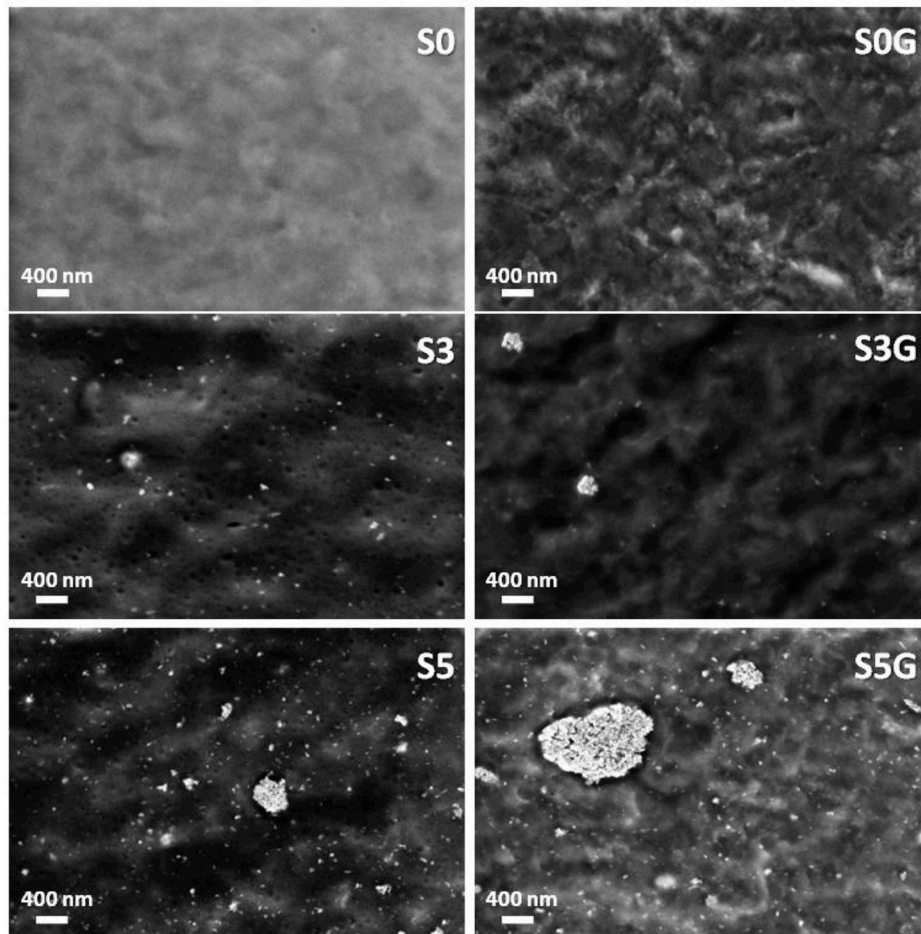
**Fig. 3.** FESEM micrographs of the nanocomposites for three selected films.

**Table 2**
Tensile properties of the films.

| Sample | $E$ (MPa) | $\sigma_u$ (MPa) | $\varepsilon_b$ (%) |
|--------|-----------|------------------|---------------------|
| S0 | 1098 ± 337[b] | 22.7 ± 7.6[a] | 14.8 ± 11.6[a] |
| S1 | 1215 ± 328[b] | 25.8 ± 6.4[a] | 17.5 ± 11.6[a] |
| S2 | 1025 ± 509[b] | 27.5 ± 6.1[a] | 11.6 ± 5.3[a] |
| S3 | 1229 ± 46[b] | 27.9 ± 3.3[a] | 11.9 ± 6.1[a] |
| S4 | 1482 ± 401[ab] | 30.4 ± 9.4[a] | 14.1 ± 7.3[a] |
| S5 | 1677 ± 108[a] | 31.1 ± 4.3[a] | 11.3 ± 6.3[a] |
| S0G | 69 ± 14[c] | 7.5 ± 1.9[bc] | 15.5 ± 5.1[a] |
| S1G | 73 ± 14[c] | 5.2 ± 0.8[c] | 8.6 ± 2.4[a] |
| S2G | 79 ± 16[c] | 5.6 ± 1.6[bc] | 8.6 ± 2.9[a] |
| S3G | 77 ± 15[c] | 8.3 ± 2.1[b] | 12.1 ± 2.3[a] |
| S4G | 60 ± 14[c] | 7.1 ± 1.5[bc] | 14.3 ± 0.9[a] |
| S5G | 79 ± 22[c] | 7.7 ± 3.3[bc] | 12.5 ± 6.5[a] |

[a,b,c] Different letters in the same column indicate significant differences ($p < 0.05$). Reported values correspond to the mean ± standard deviation.

$$V_{MNP} = \frac{v_{MNP}}{v_{film}} = \frac{\frac{W_{MNP}}{\rho_{MNP}}}{\frac{W_{MNP}}{\rho_{MNP}} + \frac{W_{matrix}}{\rho_{matrix}}} \qquad (2)$$

The density of the unfilled matrix ($\rho_{matrix} = 1.3 \, \text{g/cm}^3$) was experimentally determined as the ratio between the weight and volume of rectangular specimens, and the density of the filler ($\rho_{MNP}$) was taken as 5.175 g/cm³ [56].
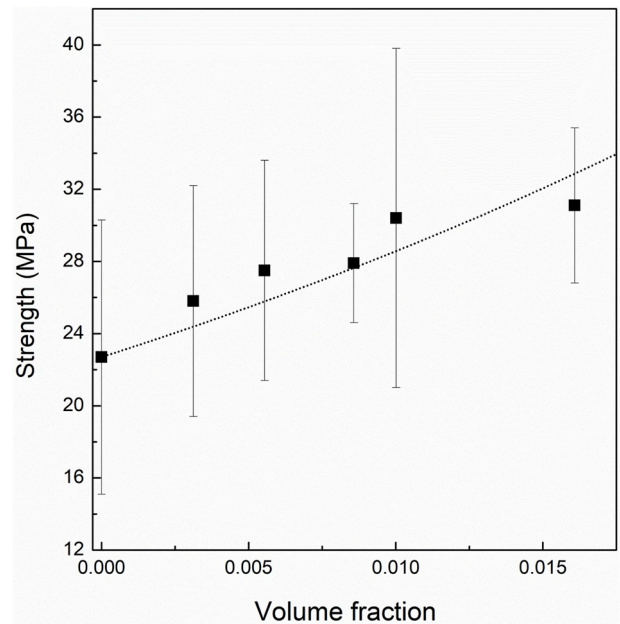


**Fig. 4.** Experimental (symbols) strength and theoretical (dash line) values calculated from the Pukanszky model as a function of MNP volume fraction.
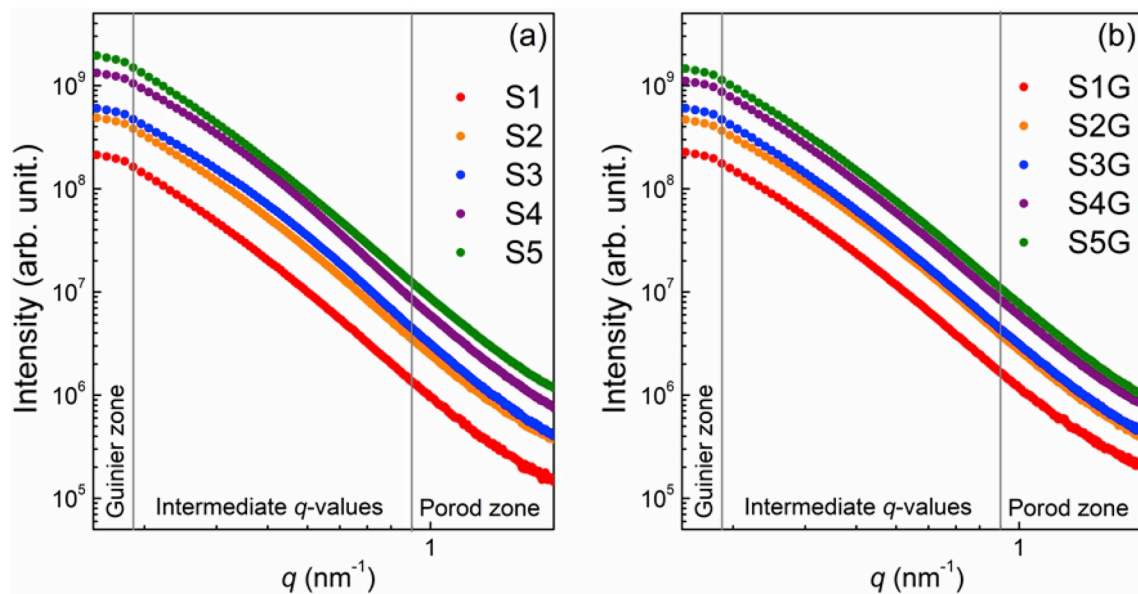
**Fig. 5.** Small angle X-ray scattering intensity (*I*) as a function of the momentum transfer vector (*q*) for non-plasticized (a) and plasticized samples (b).

Fig. 4 shows the evolution of the ultimate stress as function of volume fraction of MNP for non-plasticized films. In the same figure, the calculated fitting curve (equation (1)) is displayed. According to the fit results, a value of 26 was found for the *B* parameter, being this much larger than 3, meaning that the interface is strong and an effective reinforcing effect was obtained [57].

On the other hand, the strong plasticizing effect of the glycerol is clearly denoted by the important decrease of the rigidity of plasticized samples with respect to non-plasticized ones, resulting in lower modulus and strength values (Table 2). However, these properties do not present a clear trend with MNP concentration. Particle agglomeration could affect the effective stiffness of the particles and the load transfer at the matrix-particle interface, facts related with modulus and strength of the nanocomposites, respectively. This behavior could be attributed to the heterogeneity of the films regarding MNP concentration and probably associated with less compatibility between particles and plasticized matrix than the observed for the non-plasticized samples. This fact could be directly associated to the presence of higher agglomerates in the nanocomposites with glycerol as was previously mentioned in the analysis of FESEM images.

The ultimate deformation does not present a clear trend, neither with respect to magnetite concentration, nor with respect to glycerol content (i.e. comparing S samples with SG samples at fixed magnetite concentration).

From FESEM images analysis, it became clear that composite samples contain aggregates of individual particles. Thus, the SAXS technique was used to complement the structural information, as well as to follow the cluster formation into the chitosan based films. The range of analysis of the SAXS measurements is restricted with respect to the size of particles or structures loaded into the matrix (i.e. depends on the selected *q* range). Thus just some general information about nanostructures will be obtained and used as a comparative tool. Firstly it should be noticed that even when the FESEM images suggest the presence of at least a bimodal distribution of cluster sizes, the measured *q*-range in SAXS covers only those scattering objects matching the smaller ones.

Fig. 5 shows the Log–Log representation of scattering intensity, *I*(*q*) versus the momentum transfer, *q*, for the magnetic nanocomposites. As can be noted, the SAXS experimental curves display similar trends, where three different scattering regions can be highlighted. In low-*q* region, all spectra exhibit similar power law trends, indicating a deviation from the Guinier behavior characteristic of non-interacting

individual particles (i.e. ultra-dispersed systems). This deviation can be attributed to the scattering interference between the neighboring iron oxide NPs, denoting their aggregation into the films [58,59]. In this zone (Guinier region), for *q*–values lower than 0.1 nm$^{-1}$, a power law of $I \sim q^{-2.4}$ was found for all samples. In the high-*q* region, the scattering intensity behavior can be described with a power law $I(q) \sim q^{-\beta}$, being *β* the Porod exponent, whose values were found between −3 and −4 for all samples, characteristic of Porod scattering from smooth and sharp interfaces among iron oxide NPs and polymer matrix [60–62]. At intermediate *q*-values (0.2 nm$^{-1}$ < *q* < 0.95 nm$^{-1}$), the absence of oscillations suggests a moderate polydispersity of the MNP loaded into the chitosan matrices.

To perform a quantitative analysis, experimental SAXS curves were evaluated using the unified exponential/power-law postulated by Beaucage and based on hierarchical structures [63]. The phenomenology behind this model implies to consider a combination of the Porod and Guinier regimes to describe the scattering intensity of any systems composed by entities of complex morphology, which can contain multiple levels of related structural features. In our case, to describe two interconnected structural levels (aggregates and individual NPs), the following equation was used:

$$I(q) \cong G \exp\frac{(-q^2 R_g^2)}{3} + B \exp\frac{(-q^2 R_s^2)}{3}\left(\frac{(\mathrm{erf}(q R_g/\sqrt{6})^3}{q}\right)^{D_f}$$
$$+ Gs \exp\frac{(-q^2 R_s^2)}{3} + Bs\left(\frac{(\mathrm{erf}(q R_s/\sqrt{6})^3}{q}\right)^{P}$$
(3)

where *G* and *B* correspond to the Guinier and Porod pre-factors of those larger structures detected in the measured *q* range (aggregates); $G_s$ and $B_s$ are the Guinier and Porod pre-factors of the smaller structures (individual particles); $R_g$ is the radius of gyration of aggregates with fractal dimension $D_f$, and whose architecture is defined by small particles of size $R_s$. *P* is the exponent of the power law assigned to the smaller structures and *erf* is the error function. Notice that the first term of equation (3) describes the large-scale structure of size $R_g$, while the second one refers to the mass-fractal regime with two structural limits. The last two terms are related with the structural information of smaller substructure (primary MNPs).

The Beaucage approach was successfully applied to describe the scattering intensity from those polydispersed NPs that interact forming clusters of larger sizes into the selected matrices. The curves obtained
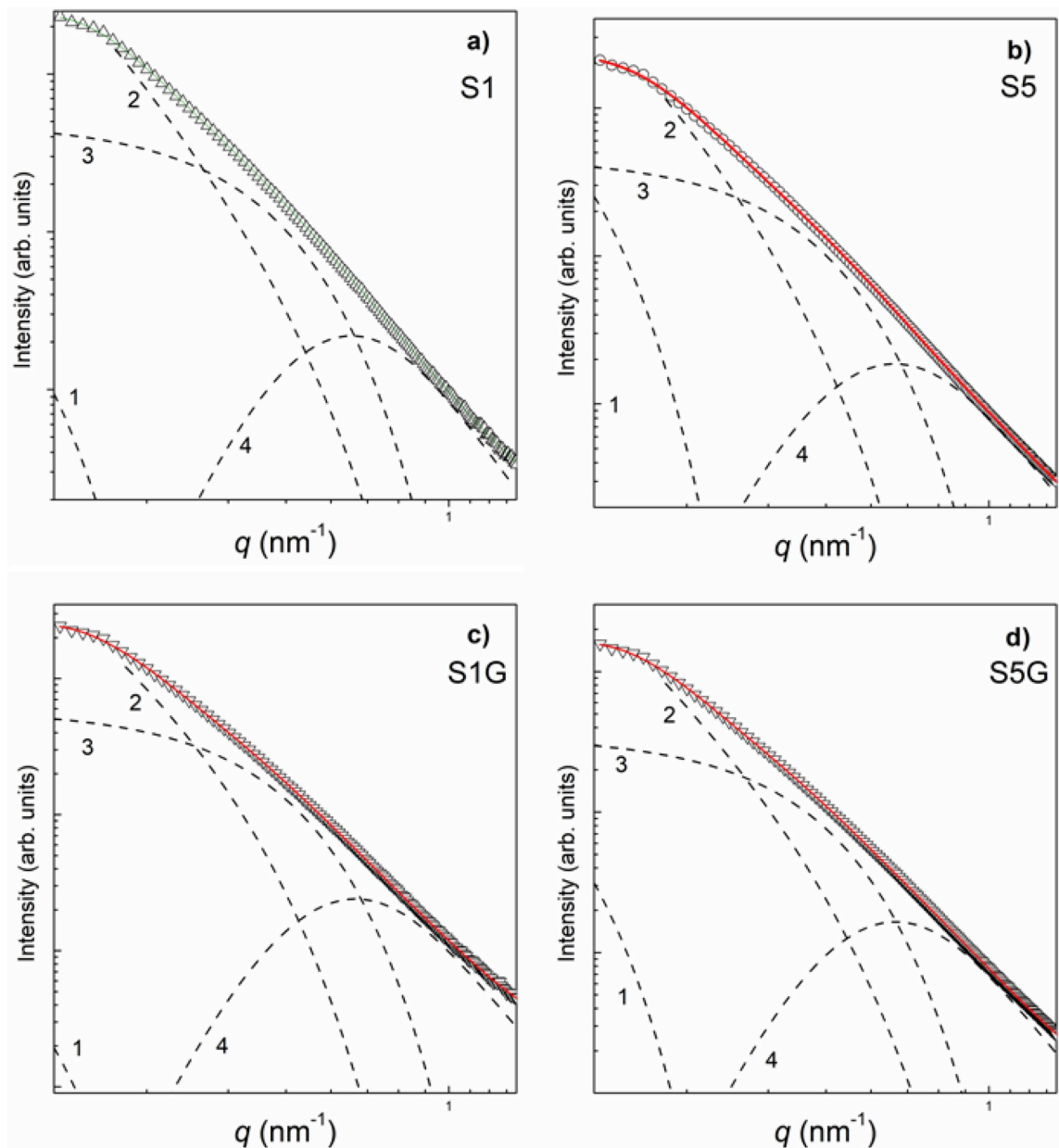
**Fig. 6.** Experimental data (empty symbols) and fitting of equation (3) with SASfit package (solid line) and the different contributions of Beaucage model. 1) Guinier aggregates, 2) Porod aggregates, 3) Guinier individual particles, 4) Porod individual particles.

**Table 3**
SAXS parameters obtained using equations (3)–(5).

$G$: Guinier pre-factor of larger structures, $B$: Porod pre-factor of larger structures, $G_s$: Guinier pre-factor of smaller structures, $B_s$: Porod pre-factor of the smaller structures, $R_g$: radius of gyration of aggregates, $D_f$: fractal dimension, $R_s$: radius of individual particles, $P$: exponent of the power law assigned to the smaller structures, $\xi$: radius of the agglomerate, $PDI$: polydispersity index, $Z$: grade of aggregation.

| Sample | $G$ | $B$ | $G_s$ | $B_s$ | $R_g$ (nm) | $R_s$ (nm) | $D_f$ | $P$ | $\xi$ (nm) | $PDI$ | $Z$ |
|---|---|---|---|---|---|---|---|---|---|---|---|
| S1 | 5.03E7 | 1.22E6 | 4.47E7 | 8.88E5 | 21.92 | 4.792 | 2.99 | 4.01 | 55.56 | 6.5 | 9.7 |
| S2 | 2.24E7 | 2.95E6 | 1.20E8 | 2.38E6 | 21.51 | 4.757 | 2.98 | 3.82 | 55.55 | 6.3 | 9.5 |
| S3 | 1.69E7 | 3.79E6 | 1.55E8 | 2.95E6 | 21.79 | 4.770 | 2.92 | 3.99 | 56.26 | 6.1 | 9.2 |
| S4 | 6.89E8 | 2.10E7 | 3.37E8 | 5.62E6 | 21.17 | 4.795 | 2.46 | 3.98 | 54.65 | 5.5 | 6.2 |
| S5 | 4.95E9 | 1.16E7 | 3.87E8 | 8.60E6 | 21.04 | 4.776 | 2.99 | 3.72 | 51.43 | 7.1 | 9.2 |
| S1G | 3.77E6 | 2.84E6 | 5.87E7 | 1.05E6 | 21.317 | 4.795 | 2.61 | 3.98 | 55.04 | 5.8 | 7.0 |
| S2G | 2.70E8 | 3.43E6 | 1.34E8 | 2.53E6 | 21.11 | 4.795 | 2.88 | 3.98 | 54.51 | 6.2 | 8.5 |
| S3G | 2.80E8 | 3.38E6 | 1.40E8 | 2.89E6 | 21.38 | 4.794 | 3.04 | 3.98 | 55.20 | 6.7 | 9.7 |
| S4G | 5.31E8 | 6.23E6 | 2.65E8 | 5.55E6 | 21.16 | 4.793 | 3.04 | 3.97 | 54.63 | 6.8 | 9.5 |
| S5G | 6.08E8 | 7.82E6 | 3.45E8 | 7.26E6 | 21.30 | 4.792 | 3.06 | 3.97 | 55.00 | 6.8 | 9.8 |
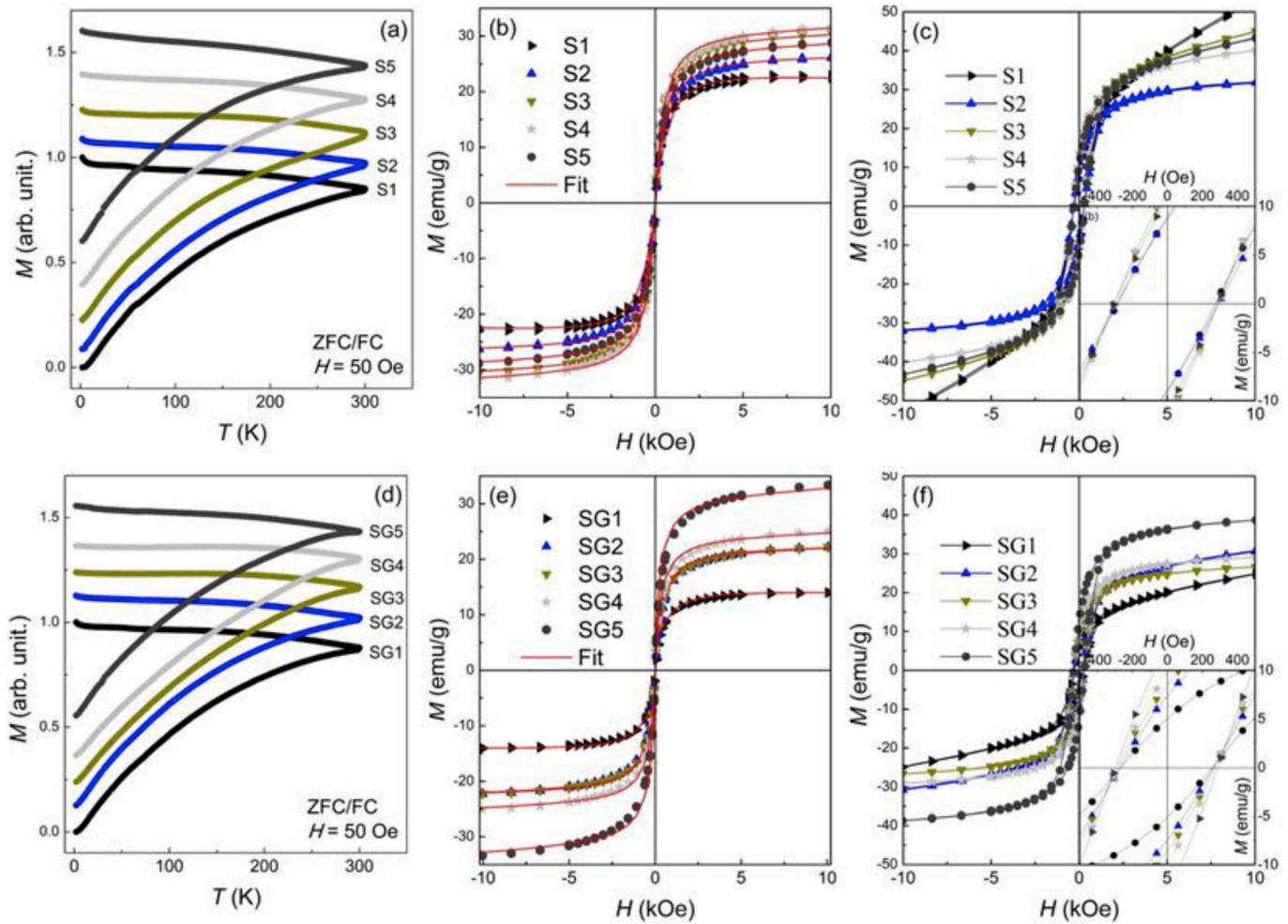
**Fig. 7.** (a) and (d) Magnetization as a function of the temperature recorded under *ZFC* and *FC* protocols for samples S and SG, respectively. *ZFC* and *FC* curves are normalized and vertically displaced for better understanding. (b) and (c) Magnetization vs. magnetic field curves at 300 and 2 K for samples S. (e) and (f) Magnetization vs. magnetic field curves at 300 and 2 K for samples SG. Continuous lines at *M* vs.*H* recorded at 300 K represent the Langevin fits. Magnetization values are presented in emu/g of magnetic material.

by fitting the model are in good agreement with experimental data, as can be observed in Fig. 6 for the samples S1, S5, S1G and S5G. The individual contributions of the Guinier and Porod component curves of aggregates (curves 1 and 2) and primary particles (curves 3 and 4) are also included in the plot (dashed lines).

Thus, equation (3) allows modeling the experimental SAXS results and determining the fitting parameters, such as $R_g$, $D_f$ and the pre-factors, $G$, $B$, $G_s$ and $B_s$ for different chitosan/MNP films (Table 3). The $P$ exponent and the single nanoparticle radius ($Rs$) were set as 4 and 4.8 nm (this last one, according to TEM information), respectively, although a relative small variation of ± 10% was allowed for fitting purposes.

Fitting parameters $G$, $B$, $G_s$ and $B_s$ (see Table 3) increase with MNP content for both, plasticized and non-plasticized samples as was expected, because they are directly related with the relative amount of iron oxide NPs ($G_s$ and $B_s$) and agglomerates ($G$ and $B$). As the amount of individual particles rises, an increase in the amount of agglomerates is expected. In addition, the pre-factors are higher for the non-plasticized samples with the most important differences in $G$ and $B$ parameters, fact that could be related with differences in the electronic contrast between the matrix and particles, when the former is plasticized or not: the presence of glycerol can modify the dispersion length densities of the matrix and consequently the electronic contrast of particular zones of the composite.

Table 3 also presents the polydispersity index, *PDI*, and the grade of aggregation, $_Z$ (defined as the amount of particles of mean radius $R_s$

contained by an aggregate of radius $R_g$) calculated by the following equations [64].

$$PDI = \frac{B_s \cdot R_s^4}{1.62 \cdot G_s} \tag{4}$$

$$Z = \left(\frac{R_s}{R_g}\right)^{-D_f/2} \tag{5}$$

Since $D_f$ is a parameter of the fractal dimension, their values, quite similar for all films, indicate that in all the samples the agglomerates of individual particles have similar structures. Their values are mostly close to 3, indicating tridimensional smooth and compact clusters [65] with a tridimensional architecture. On the other hand, $R_g$, which stands for the aggregate sizes, does not suffer significant variation with the concentration of MNP. Assuming that the shape of the agglomerates is spherical, their sizes can be calculated using $\xi = 2(5/3)^{1/2}R_g$.

Fig. 7 shows a general overview of the DC magnetic properties in the investigated nanocomposite films. The temperature dependence of magnetization for different samples is displayed in Fig. 7 (a) and (d); these curves were recorded at a low DC field of 50 Oe under the zero-field-cooling and field-cooling protocols. As can be noted, all the ZFC/FC curves show a similar behavior, where the *ZFC* magnetization curves progressively increases without a defined maximum in the range of analyzed temperatures, while, the *FC* curves show a monotonous

**Table 4**

Best fitting parameters according to equation (6) and coercive fields obtained from the $M$ vs. $H$ curves recorded at 2 K.

$\sigma$: variance, $\mu_M$: magnetic moment per magnetic entity, $N$ the number of monodomain entities per unit mass, $H_C$: coercive field.

| Sample | $\sigma$ | $\mu_M$ ($10^3\mu_B$) | $N$ ($10^{17}$cm$^{-3}$) | $H_C$ (Oe) at 2 K |
|--------|----------|----------------------|--------------------------|--------------------|
| S1 | 0.3 | 11.8 | 2.2 | 280 |
| S2 | 0.4 | 11.9 | 2.1 | 290 |
| S3 | 0.6 | 12.4 | 2.2 | 295 |
| S4 | 0.6 | 12.6 | 2.2 | 298 |
| S5 | 0.5 | 12.5 | 2.2 | 297 |
| SG1 | 1.0 | 6.7 | 1.5 | 260 |
| SG2 | 0.8 | 10.7 | 1.6 | 265 |
| SG3 | 0.8 | 11.1 | 1.6 | 276 |
| SG4 | 0.8 | 13.1 | 1.4 | 278 |
| SG5 | 0.9 | 14.3 | 1.6 | 290 |

decrease as temperature rises. Moreover, *ZFC* and *FC* joint near to 300 K, which indicates that both blocking and irreversibility temperatures are probably close to room temperature. These are characteristics for highly or moderate interacting nanoparticulated systems, with a broad size distribution and where not all the NPs become unblocked at 300 K [66].

Isothermal hysteresis loops were measured in all nanocomposites at two different temperatures (2 K and 300 K). According to our results, every $M$ vs. $H$ curve obtained at 300 K (Fig. 7(b) and (e)) displays a *S*-shape with an almost null coercive field ($H_C$) i.e., absence of hysteresis. This is a typical feature of granular systems composed by monodomain NPs, as explained by Allia et al. [67] and Knobel et al. [68]. Besides, the magnetization values obtained at 2 K are larger than the ones measured at 300 K. Despite that the magnetization curves of both systems (plasticized and not plasticized) share some similarities, there are differences in the magnetization saturation ($M_S$) values. For instance, comparing the $M$ vs. $H$ curves measured at 300 K, those films loaded with lowest NP concentrations, i.e., S1 and SG1, take values of *Ms* around ~21 emu/g and 18 emu/g (normalized per MNP mass), respectively. On the other hand, in samples S5 and SG5 (nanocomposites films with highest NP concentration), the *Ms* have values of 27 and 35 emu/g, respectively. Thus, for both sets of analyzed magnetic nanocomposite films one can distinguish an increase of $M_S$ as the concentration of magnetic solute rises from samples 1 to 5.

This behavior seems to be dependant on the NPs concentration, where aggregates features, such as size and compactness degree, are directly influenced by the amount of magnetic solute (as was inferred from SAXS and FESEM analysis). In addition, the aggregate formations lead to different collective behaviors among NPs, which should be related to cluster features. These facts can reveal the formation of systems with differences in dipolar interactions and effective anisotropies, which affect the magnetization dynamics, and, consequently, the corresponding macroscopic parameters (such as $M_S$ and/or $H_C$) [69]. It is worth noting that all the $M$ vs. $H$ curves display lower values of $M_S$, when compared to those reported for bulk magnetite [70]. This behavior can be understood considering the disorder on the nanoparticle surface [71]. Comparing the magnetization behavior of the two sets of systems, differences between the $M_S$ values of samples S and SG for a specific concentration can easily perceived, suggesting different aggregation of the NPs. This effect can be affected by the interaction among the functional groups of the matrix and the active chemical groups located at the interface of the nanoparticle, as suggested in previous works [52,72]. Table 4 listes the coercive field values ($H_C$) extracted from the $M$ vs. $H$ curves obtained at 2 K. For both systems (S and SG) it can be noticed that $H_C$ tends to higher values as the temperature decrease, which is an experimental evidence that the NPs are in the blocked regime at 2 K consistent with ZFC and FC results [59,73]. Furthermore, for each nanoparticle concentration, lower values of $H_C$ can be observed for plasticized samples (SG) in comparison to the other

ones. This behavior could indicate the formation of aggregates with low compactness degree.

In order to perform a quantitative analysis of the above discussed facts, we applied the Langevin formulation to fit the $M$ vs. $H$ curves measured at 300 K. Briefly, the magnetization response as a function of the magnetic field for granular nanoparticle systems can be described by the Langevin function $M = M_S L(\mu H/k_B T)$, being $\mu$ the magnetic moment per monodomain entity, $k_B$ the Boltzmann constant and $M_S$ the saturation magnetization, that also can be expressed as $M_S = N\mu$, $N$ being the number of monodomain entities per unit mass. To take into account the moment distribution (related to the presence of a particle size distribution), Langevin function was weighted by a lognormal distribution function $f(\mu)$ with median $\mu_M$ ($= \mu \exp(\sigma^2/2)$), being $\sigma$ the standard deviation. Then, the $M$ vs. $H$ data were fitted by:

$$M(H) = N \int_0^\infty \mu L\left(\frac{\mu H}{k_B T}\right) f(\mu) d\mu + C, \tag{6}$$

where the last term $C$ is a constant that contains the paramagnetic contributions that come from the nanoparticle surface disorder. The fitted curves are displayed as full lines in Fig. 7 ((b) and (e)) and the fitted parameters are summarized in Table 4. To interpret the fitting results, it must be considered that the framework behind the Langevin formulation is based on ideal systems, i.e., non-interacting and monodomain entities with moderate size distribution. However, a re-interpretation of the obtained results can support the hypothesis that the formation of aggregates with different features (each one acting as a magnetic entity) dominates the magnetization response. Accordingly, the obtained parameters, $\sigma$ and $N$, do not vary widely, while for the two investigated sets of samples, the mean magnetic moment per magnetic entity ($\mu_M$) present an increase as the nanoparticle concentration increase; for instance, $\mu_M$ of 11.8 $\mu_B$ and 6.7 $\mu_B$ were obtained for samples S1 and S1G, respectively, while for the most concentrated samples (S5 and S5G), values of 12.5 $\mu_B$ and 14.3 $\mu_B$ were found. The observed variance of $\mu_M$ can be understood from the NP arrangement (size and compactness degree) that forms each aggregate.

On samples with lower magnetic solute, it seems that the NPs are randomly arranged to give rise to structures of shorter magnetic size. On the contrary, in samples with high nanoparticle concentration, it seems that the NPs that form the aggregates are organized so that their magnetic moments are forming cooperative magnetic systems, leading to more compact structures with a bigger net magnetic moment. Theses hypothesis could suggest a cooperative-type arrangement of those magnetic moments that belong to the percolated NPs (high nanoparticle concentrations). Such hypothesis also implies that for larger NP concentration, the super-paramagnetic features of the system can be lost, which result in a magnetic response governed by the aggregates characteristics.

## 4. Conclusions

A procedure to obtain magnetic nanocomposite films using a biopolymeric matrix (chitosan) and magnetic nanoparticles was reported. The nanoparticles of iron oxides were synthesized by an alkaline co-precipitation method that leads to the formation of magnetite and/or maghemite particles of less than 10 nm average diameter. FESEM micrographs, tensile tests, magnetic properties and SAXS analysis were used to evaluate film specific properties, but also to obtain indirect information regarding film's nano and microstructure.

The mechanical behavior under uniaxial tensile tests was associated to a good interaction nanoparticles-matrix, mainly for the non-plasticized samples where a clear reinforcing effect was observed.

Magnetic results showed that the nanoparticles within the films are super-paramagnetic, with blocking temperatures close to room temperature. Generally speaking, the magnetic response was dominated by the collective behavior of interacting dipolar nanoparticles associated

with the presence of aggregates with variations in sizes and compactness degree. The aggregation of individual magnetic particles in the composite films was corroborated from FESEM images, with the larger ones found in the plasticized samples. SAXS data were successfully fitted with the Beaucage model and the calculated parameters denoted the existence of volume fractal dimensions in the smaller clusters.

In conclusion, these nanocomposites are excellent candidates for a wide range of applications, owing to (i) easy access and low cost of raw materials and processing, (ii) the low toxicity of chitosan, MNP and the solvent used (water), (iii) the chelating characteristics inherent to chitosan and magnetic nanoparticles.

## Data availability

The raw/processed data required to reproduce these findings cannot be shared at this time as the data also forms part of an ongoing study.

## Acknowledgements

## Appendix A. Supplementary data

Supplementary data to this article can be found online at https://doi.org/10.1016/j.polymertesting.2018.10.022.

## References

[1] S.M. Husnain, W. Um, Magnetite-based adsorbents for sequestration of radionuclides : a review, RSC Adv. 8 (2018) 2521–2540, https://doi.org/10.1039/C7RA12299C.

[2] N.A. Pattanashetti, G.B. Heggannavar, M.Y. Kariduraganavar, Smart biopolymers and their biomedical applications, Procedia Manufacturing 12 (2017) 263–279, https://doi.org/10.1016/j.promfg.2017.08.030.

[3] D.W. Cho, B.H. Jeon, C.M. Chon, Y. Kim, F.W. Schwartz, E.S. Lee, H. Song, A novel chitosan/clay/magnetite composite for adsorption of Cu(II) and As(V), Chem. Eng. J. 200–202 (2012) 654–662, https://doi.org/10.1016/j.cej.2012.06.126.

[4] E. Alver, M. Bulut, H. Çiftçi, Molecular and biomolecular spectroscopy one step effective removal of Congo Red in chitosan nanoparticles by encapsulation, Spectrochim. Acta, Part A 171 (2017) 132–138.

[5] M. Agostini de Moraes, D.S. Cocenza, F. da Cruz Vasconcellos, L.F. Fraceto, M.M. Beppu, Chitosan and alginate biopolymer membranes for remediation of contaminated water with herbicides, J. Environ. Manag. 131 (2013) 222–227, https://doi.org/10.1016/j.jenvman.2013.09.028.

[6] A. Rafiee, M.H. Alimohammadian, T. Gazori, F. Riazi-rad, S.M.R. Fatemi, A. Parizadeh, I. Haririan, M. Havaskary, Comparison of chitosan, alginate and chitosan/alginate nanoparticles with respect to their size, stability, toxicity and transfection, Asian Pacific Journal of Tropical Disease 4 (2014) 372–377, https://doi.org/10.1016/S2222-1808(14)60590-9.

[7] A.F. Martins, P.V.A. Bueno, E.A.M.S. Almeida, F.H.A. Rodrigues, A.F. Rubira, E.C. Muniz, Characterization of N-trimethyl chitosan/alginate complexes and curcumin release, Int. J. Biol. Macromol. 57 (2013) 174–184, https://doi.org/10.1016/j.ijbiomac.2013.03.029.

[8] G.L. Dotto, V.C. de Souza, J.M. de Moura, C.M. de Moura, L.A. de Almeida Pinto, Influence of drying techniques on the characteristics of chitosan and the quality of biopolymer films, Dry. Technol. 29 (2011) 1784–1791, https://doi.org/10.1080/07373937.2011.602812.

[9] K. Yu, J. Ho, E. McCandlish, B. Buckley, R. Patel, Z. Li, N.C. Shapley, Copper ion adsorption by chitosan nanoparticles and alginate microparticles for water purification applications, Colloid. Surface. Physicochem. Eng. Aspect. 425 (2013) 31–41, https://doi.org/10.1016/j.colsurfa.2012.12.043.

[10] H.V. Tran, L.D. Tran, T.N. Nguyen, Preparation of chitosan/magnetite composite beads and their application for removal of Pb(II) and Ni(II) from aqueous solution, Mater. Sci. Eng. C 30 (2010) 304–310, https://doi.org/10.1016/j.msec.2009.11.008.

[11] P. Xu, G.M. Zeng, D.L. Huang, C.L. Feng, S. Hu, M.H. Zhao, C. Lai, Z. Wei, C. Huang, G.X. Xie, Z.F. Liu, Use of iron oxide nanomaterials in wastewater treatment: a review, Sci. Total Environ. 424 (2012) 1–10, https://doi.org/10.1016/j.scitotenv.2012.02.023.

[12] K.J. Sreeram, M. Nidhin, B.U. Nair, Synthesis of aligned hematite nanoparticles on chitosan-alginate films, Colloids Surfaces B Biointerfaces 71 (2009) 260–267, https://doi.org/10.1016/j.colsurfb.2009.02.015.

[13] F. Zhuang, R. Tan, W. Shen, X. Zhang, W. Xu, W. Song, Magnetic strontium hydroxyapatite microspheres for the efficient removal of Pb ( II ) from acidic solutions, J. Chem. Eng. Data 59 (2014) 3873–3881.

[14] A.E. Regazzoni, G.A. Urrutia, M.A. Blesa, A.J.G. Maroto, Some observations on the composition and morphology of synthetic magnetites obtained by different routes, J. Inorg. Nucl. Chem. 43 (1981) 1489–1493, https://doi.org/10.1016/0022-1902(81)80322-3.

[15] D.J. Shaw, Introduction to Colloid and Surface Chemistry, Butterworth Heinemann (a division of Reed Educational and Professional Publishers), Woburn, USA, 1992.

[16] M. Lavorgna, F. Piscitelli, P. Mangiacapra, G.G. Buonocore, Study of the combined effect of both clay and glycerol plasticizer on the properties of chitosan films, Carbohydr. Polym. 82 (2010) 291–298, https://doi.org/10.1016/j.carbpol.2010.04.054.

[17] A. Zhu, L. Yuan, T. Liao, Suspension of $Fe_3O_4$ nanoparticles stabilized by chitosan and o-carboxymethylchitosan, Int. J. Pharm. 350 (2008) 361–368, https://doi.org/10.1016/j.ijpharm.2007.09.004.

[18] F. Cesano, G. Fenoglio, L. Carlos, R. Nisticò, One-step synthesis of magnetic chitosan polymer composite films, Appl. Surf. Sci. 345 (2015) 175–181.

[19] O. Bezdorozhev, T. Kolodiazhnyi, O. Vasylkiv, Precipitation synthesis and magnetic properties of self-assembled magnetite-chitosan nanostructures, J. Magn. Magn Mater. 428 (2017) 406–411, https://doi.org/10.1016/j.jmmm.2016.12.048.

[20] J. Singh, M. Srivastava, J. Dutta, P.K. Dutta, Preparation and properties of hybrid monodispersed magnetic $\alpha$-$Fe_2O_3$ based chitosan nanocomposite film for industrial and biomedical applications, Int. J. Biol. Macromol. 48 (2011) 170–176, https://doi.org/10.1016/j.ijbiomac.2010.10.016.

[21] A.S. Bhatt, D. Krishna Bhat, M.S. Santosh, Electrical and magnetic properties of chitosan-magnetite nanocomposites, Phys. B Condens. Matter 405 (2010) 2078–2082, https://doi.org/10.1016/j.physb.2010.01.106.

[22] M. Knobel, L.M. Socolovsky, J.M. Vargas, Propiedades magnéticas y de transporte de sistemas nanocristalinos : conceptos básicos y aplicaciones a sistemas reales, Rev. Mexic. Fisica 50 (2004) 8–28.

[23] R. Fu, Y. Yan, C. Roberts, Z. Liu, Y. Chen, The role of dipole interactions in hyperthermia heating colloidal clusters of densely-packed superparamagnetic nanoparticles, Sci. Rep. 8 (2018) 1, https://doi.org/10.1038/s41598-018-23225-5.

[24] G.A. Kloster, D. Muraca, C. Meiorin, K.R. Pirota, N.E. Marcovich, M.A. Mosiewicki, Magnetic characterization of chitosan – magnetite nanocomposite films, Eur. Polym. J. 72 (2015) 202–211, https://doi.org/10.1016/j.eurpolymj.2015.09.014.

[25] G.A. Kloster, N.E. Marcovich, M.A. Mosiewicki, Composite films based on chitosan and nanomagnetite, Eur. Polym. J. 66 (2015) 386–396, https://doi.org/10.1016/j.eurpolymj.2015.02.042.

[26] R. Massart, V. Cabuil, Synthèse en milieu alcalin de magnétite colloïdale: contrôle du rendement et de la taille des particules, Journal de Chimie Physique 84 (1987) 967–973.

[27] C. Meiorin, D. Muraca, K.R. Pirota, M.I. Aranguren, M.A. Mosiewicki, Nanocomposites with superparamagnetic behavior based on a vegetable oil and magnetite nanoparticles, Eur. Polym. J. 53 (2014) 90–99, https://doi.org/10.1016/j.eurpolymj.2014.01.018.

[28] Y. Peng, C. Park, J. Zhu, R.M. White, D.E. Laughlin, Y. Peng, C. Park, J. Zhu, R.M. White, D.E. Laughlin, Characterization of interfacial reactions in magnetite tunnel junctions with transmission electron microscopy, J. Appl. Phys. 95 (2004) 6798–6800, https://doi.org/10.1063/1.1688535.

[29] L. Zhang, R. He, H. Gu, Oleic acid coating on the monodisperse magnetite nanoparticles, Appl. Surf. Sci. 253 (2006) 2611–2617, https://doi.org/10.1016/j.apsusc.2006.05.023.

[30] G. Schmid, Nanoparticles: from Theory to Application, Second, Wiley, 2005.

[31] M. González, I. Martín-fabiani, J. Baselga, J. Pozuelo, Magnetic nanocomposites based on hydrogenated epoxy resin, Mater. Chem. Phys. 132 (2012) 618–624, https://doi.org/10.1016/j.matchemphys.2011.11.077.

[32] P. Scherrer, Göttinger nachrichten gesell, J. Math. Phys. 2 (1918) 98.

[33] A.R. Lang, X-ray diffraction procedures for polycrystal-line and amorphous materials, Acta Metall. 4 (1956) 102, https://doi.org/10.1016/0001-6160(56)90124-9.

[34] A.L. Patterson, The Scherrer formula for X-ray particle size determination, Phys. Rev. 56 (1939) 978.

[35] A. Labarta, X. Batlle, O. Iglesias, Surface Effects in Magnetic Nanoparticles, Springer Science & Business Media, New York, 2005, https://doi.org/10.1017/CBO9781107415324.004.

[36] A.V. Teixeira, I. Morfin, P. Panine, P. Licinio, E. Geissler, Structure and magnetic properties of dilute ferrofluids suspended in gels, Compos. Sci. Technol. 63 (2003) 1105–1111, https://doi.org/10.1016/S0266-3538(03)00031-9.

[37] O. Kratky, G. Porod, Die Abhängigkeit der Röntgen-Kleinwinkelstreuung von Form und Grösse der kolloiden Teilchen in verdünnten Systemen: III, Acta Phys. Austriaca 2 (1948) 133.

[38] K. Cendrowski, P. Sikora, B. Zielinska, E. Horszczaruk, Chemical and thermal stability of core-shelled magnetite nanoparticles and solid silica, Appl. Surf. Sci. 407 (2017) 391–397, https://doi.org/10.1016/j.apsusc.2017.02.118.

[39] E.R. Monazam, R.W. Breault, R. Siriwardane, Kinetics of magnetite ($Fe_3O_4$) oxidation to hematite ($Fe_2O_3$) in air for chemical looping combustion, Ind. Eng. Chem. Res. 53 (2014) 13320–13328, https://doi.org/10.1021/ie501536s.

[40] S.F. Wang, L. Shen, Y.J. Tong, L. Chen, I.Y. Phang, P.Q. Lim, T.X. Liu, Biopolymer chitosan/montmorillonite nanocomposites: preparation and characterization, Polym. Degrad. Stabil. 90 (2005) 123–131, https://doi.org/10.1016/j.polymdegradstab.2005.03.001.

[41] M.V. Debandi, C. Bernal, N.J. Francois, Development of biodegradable films based on chitosan/glycerol blends suitable for biomedical applications, J. Tissue Sci. Eng. 07 (2016), https://doi.org/10.4172/2157-7552.1000187.

[42] J.F. Fundo, A.C. Galvis-Sanchez, I. Delgadillo, C.L.M. Silva, M.A.C. Quintas, The effect of polymer/plasticiser ratio in film forming solutions on the properties of chitosan films, Food Biophys. 10 (2015) 324–333, https://doi.org/10.1007/s11483-015-9394-3.

[43] S. Rivero, M.A. García, A. Pinotti, Correlations between structural, barrier, thermal and mechanical properties of plasticized gelatin films, Innovat. Food Sci. Emerg. Technol. 11 (2010) 369–375, https://doi.org/10.1016/j.ifset.2009.07.005.

[44] K. Okuyama, K. Noguchi, T. Miyazawa, T. Yui, K. Ogawa, Molecular and crystal structure of hydrated chitosan, Macromolecules 30 (1997) 5849–5855, https://doi.org/10.1021/ma970509n.

[45] G.D. Soto, C. Meiorin, D. Actis, P. Mendoza Zélis, M.A. Mosiewicki, N.E. Marcovich, Nanocomposites with shape memory behavior based on a segmented polyurethane and magnetic nanostructures, Polym. Test. 65 (2018) 360–368, https://doi.org/10.1016/j.polymertesting.2017.12.012.

[46] V. Bertolino, G. Cavallaro, G. Lazzara, S. Milioto, F. Parisi, Halloysite nanotubes sandwiched between chitosan layers: novel bionanocomposites with multilayer structures, New J. Chem. 42 (2018) 8384–8390, https://doi.org/10.1039/c8nj01161c.

[47] X.Q. Xu, H. Shen, J.R. Xu, M.Q. Xie, X.J. Li, The colloidal stability and core-shell structure of magnetite nanoparticles coated with alginate, Appl. Surf. Sci. 253 (2006) 2158–2164, https://doi.org/10.1016/j.apsusc.2006.04.015.

[48] G.A. Kloster, D. Muraca, M.A. Mosiewicki, N.E. Marcovich, Magnetic composite films based on alginate and nano-iron oxide particles obtained by synthesis "in situ", Eur. Polym. J. 94 (2017) 43–55.

[49] A. Moeini, A. Cimmino, G. Dal Poggetto, M. Di Biase, A. Evidente, M. Masi, P. Lavermicocca, F. Valerio, A. Leone, G. Santagata, M. Malinconico, Effect of pH and TPP concentration on chemico-physical properties, release kinetics and anti-fungal activity of Chitosan-TPP-Ungeremine microbeads, Carbohydr. Polym. 195 (2018) 631–641, https://doi.org/10.1016/j.carbpol.2018.05.005.

[50] M. Ziegler-Borowska, D. Chełminiak, H. Kaczmarek, A. Kaczmarek-Kędziera, Effect of side substituents on thermal stability of the modified chitosan and its nano-composites with magnetite, J. Therm. Anal. Calorim. 124 (2016) 1267–1280, https://doi.org/10.1007/s10973-016-5260-x.

[51] M. Ziegler-Borowska, D. Chełminiak, H. Kaczmarek, Thermal stability of magnetic nanoparticles coated by blends of modified chitosan and poly(quaternary ammonium) salt, J. Therm. Anal. Calorim. 119 (2015) 499–506, https://doi.org/10.1007/s10973-014-4122-7.

[52] O. Moscoso-Londoño, D. Muraca, L.A.S. De Oliveira, K.R. Pirota, L.M. Socolovsky, The effect of coated- nanoparticles on magnetic properties of ferrogels produced by diffusion route, IEEE Trans. Magn. 49 (2013) 4551–4554.

[53] M. Mosiewicki, J. Borrajo, M.I. Aranguren, Mechanical properties of woodflour/linseed oil resin composites, Polym. Int. 54 (2005) 829–836, https://doi.org/10.1002/pi.1778.

[54] U. Casado, N.E. Marcovich, M.I. Aranguren, M.A. Mosiewicki, High-strength composites based on tung oil polyurethane and wood flour: effect of the filler concentration on the mechanical properties, Polym. Eng. Sci. 49 (2009) 713–721, https://doi.org/10.1002/pen.

[55] B. Pukánszky, F. Tüdös, J. Jančař, J. Kolařik, The possible mechanisms of polymer-filler interaction in polypropylene-CaCO₃ composites, J. Mater. Sci. Lett. 8 (1989) 1040–1042, https://doi.org/10.1007/BF01730480.

[56] J.W. Anthony, R.A. Bideaux, W.B. Kenneth, C.N. Monte, Handbook of Mineralogy, Mineralogical Society of America, Chantilly, 2011.

[57] J.R.M. D'Almeida, L.H. De Carvalho, An investigation on the tensile strength of particulate filled polymeric composites, J. Mater. Sci. 33 (1998) 2215–2219, https://doi.org/10.1023/A:1004348025804.

[58] M.B. Fernández van Raap, P. Mendoza Zélis, D.F. Coral, T.E. Torres, C. Marquina, G.F. Goya, F.H. Sánchez, Self organization in oleic acid-coated CoFe₂O₄ colloids: a SAXS study, J. Nanoparticle Res. 14 (2012) 1072, https://doi.org/10.1007/s11051-012-1072-5.

[59] O. Moscoso-Londoño, P. Tancredi, D. Muraca, P. Mendoza Zélis, D. Coral, M.B. Fernández van Raap, U. Wolff, V. Neu, C. Damm, C.L.P. de Oliveira, K.R. Pirota, M. Knobel, L.M. Socolovsky, Different approaches to analyze the di-polar interaction effects on diluted and concentrated granular superparamagnetic systems, J. Magn. Magn Mater. 428 (2017) 105–118, https://doi.org/10.1016/j.jmmm.2016.12.019.

[60] O. Moscoso-Londoño, P. Tancredi, D. Muraca, P.M. Zélis, D. Coral, M.B.F. Van Raap, U. Wol, V. Neu, C. Damm, C.L.P. De Oliveira, K.R. Pirota, Different approaches to analyze the dipolar interaction effects on diluted and concentrated granular su-perparamagnetic systems, J. Magn. Magn Mater. 428 (2017) 105–118, https://doi.org/10.1016/j.jmmm.2016.12.019.

[61] O. Glatter, O. Kratky, Small Angle X-ray Scattering, Academic Press, New York, 1982.

[62] R. Hernández, J. Sacristán, A. Nogales, T.A. Ezquerra, C. Mijangos, Structural or-ganization of iron oxide nanoparticles synthesized inside hybrid polymer gels de-rived from alginate studied with small-angle X-ray scattering, Langmuir 25 (2009) 13212–13218, https://doi.org/10.1021/la902441s.

[63] G. Beaucage, Approximations leading to a unified exponential/power-law approach to small-angle scattering, J. Appl. Crystallogr. 28 (1995) 717–728, https://doi.org/10.1107/S0021889895005292.

[64] G. Beaucage, H.K. Kammler, S.E. Pratsinis, Particle size distributions from small-angle scattering using global scattering functions research papers, J. Appl. Crystallogr. (2004) 523–535, https://doi.org/10.1107/S0021889804008969.

[65] S.-H. Chen, J. Teixeira, Structure and fractal dimension of protein-detergent com-plexes, Phys. Rev. Lett. 57 (1986) 2583–2586, https://doi.org/10.1103/PhysRevLett.57.2583.

[66] L.M. Socolovsky, O. Moscoso Londoño, Complex Magnetic Nanostructures. Consequences of Magnetic Interaction Phenomena in Granular Systems, Springer, Cham, 2017.

[67] P. Allia, M. Coisson, P. Tiberto, F. Vinai, M. Knobel, M. Novak, W. Nunes, Granular Cu-Co alloys as interacting super paramagnets, Phys. Rev. B 64 (2001) 1–12, https://doi.org/10.1103/PhysRevB.64.144420.

[68] M. Knobel, W.C. Nunes, L.M. Socolovsky, E. De Biasi, J.M. Vargas, J.C. Denardin, Superparamagnetism and other magnetic features in granular materials: a review on ideal and real systems, J. Nanosci. Nanotechnol. 8 (2008) 2836–2857, https://doi.org/10.1166/jnn.2008.

[69] P.C. Rivas Rojas, P. Tancredi, O.M. Londoño, M. Knobel, L.M. Socolovsky, Tuning dipolar magnetic interactions by controlling individual silica coating of iron oxide nanoparticles, J. Magn. Magn Mater. 451 (2018) 688–696, https://doi.org/10.1016/j.jmmm.2017.11.099.

[70] D.H. Han, J.P. Wang, H.L. Luo, Crystallite size effect on saturation magnetization of fine ferrimagnetic particles, J. Magn. Magn Mater. 136 (1994) 176–182.

[71] M.P. Morales, S. Veintemillas-Verdaguer, M.I. Montero, C.J. Serna, A. Roig, L. Casas, B. Martínez, F. Sandiumenge, Surface and internal spin canting in γ-Fe₂O₃ nanoparticles, Chem. Mater. 11 (1999) 3058–3064, https://doi.org/10.1021/cm991018f.

[72] C. Meiorin, O.M. Londoño, D. Muraca, L.M. Socolovsky, K.R. Pirota, M.I. Aranguren, M. Knobel, M.A. Mosiewicki, Magnetism and structure of nano-composites made from magnetite and vegetable oil based polymeric matrices, Mater. Chem. Phys. 175 (2016) 81–91, https://doi.org/10.1016/j.matchemphys.2016.02.071.

[73] J.M. Vargas, W.C. Nunes, L.M. Socolovsky, M. Knobel, D. Zanchet, Effect of dipolar interaction observed in iron-based nanoparticles, Phys. Rev. B Condens. Matter 72 (2005) 2–7, https://doi.org/10.1103/PhysRevB.72.184428.